

1 **Title: SARS-CoV-2 spike D614G variant confers enhanced replication and transmissibility**

2

3 Bin Zhou ^{¶,1}, Tran Thi Nhu Thao ^{¶,2,3,4}, Donata Hoffmann ^{¶,5}, Adriano Taddeo ^{¶,2,3}, Nadine
4 Ebert^{2,3}, Fabien Labroussaa^{3,6}, Anne Pohlmann⁵, Jacqueline King⁵, Jasmine Portmann^{2,3}, Nico
5 Joel Halwe⁵, Lorenz Ulrich⁵, Bettina Salome Trüeb^{3,6}, Jenna N. Kelly^{2,3}, Xiaoyu Fan¹, Bernd
6 Hoffmann⁵, Silvio Steiner^{2,3,4}, Li Wang¹, Lisa Thomann^{2,3}, Xudong Lin⁷, Hanspeter Stalder^{2,3},
7 Berta Pozzi⁸, Simone de Brot⁹, Nannan Jiang¹⁰, Dan Cui⁷, Jaber Hossain¹, Malania Wilson¹,
8 Matthew Keller¹, Thomas J. Stark¹, John R. Barnes¹, Ronald Dijkman^{2,3,11}, Joerg Jores^{3,6} Charaf
9 Benarafa ^{§,*2,3}, David E. Wentworth ^{§,*1}, Volker Thiel ^{§,*2,3}, Martin Beer ^{§,*5}

10

11 ¹*CDC COVID-19 Response, Centers for Disease Control and Prevention, Atlanta, Georgia,
12 United States of America*

13 ²*Institute of Virology and Immunology (IVI), Bern and Mittelhäusern, Switzerland*

14 ³*Department of Infectious Diseases and Pathobiology, Vetsuisse Faculty, University of Bern,
15 Bern, Switzerland*

16 ⁴*Graduate School for Biomedical Science, University of Bern, Bern, Switzerland*

17 ⁵*Institute of Diagnostic Virology, Friedrich-Loeffler-Institut, Greifswald-Insel Riems, Germany*

18 ⁶*Institute of Veterinary Bacteriology, Vetsuisse Faculty, University of Bern, Bern, Switzerland*

19 ⁷*Battelle Memorial Institute, Atlanta, Georgia, United States of America*

20 ⁸*Institute of Cell Biology, University of Bern, Bern, Switzerland*

21 ⁹COMPATH, Institute of Animal Pathology, University of Bern, Bern, Switzerland

22 ¹⁰Oak Ridge Institute for Science and Education, Oak Ridge, Tennessee, United States of
23 America

24 ¹¹Institute for Infectious Diseases, University of Bern, Bern, Switzerland

25

26 [¶]: these authors contributed equally

27 [§]: these authors jointly supervised

28 *corresponding authors:

29 Volker Thiel; e-mail: volker.thiel@vetsuisse.unibe.ch; phone: +41-31-6312413

30 Martin Beer; e-mail: martin.beer@fli.de; phone: +49-38351-71200

31 David E. Wentworth; email: dwentworth@cdc.gov; phone: +1 404-639-3387

32 Charaf Benarafa; charaf.benarafa@vetsuisse.unibe.ch; +41-58-4699246

33 Abstract: 157 words ; main text : 2467 words.

34

35

36 **Abstract**

37

38 During the evolution of SARS-CoV-2 in humans a D614G substitution in the spike (S) protein
39 emerged and became the predominant circulating variant (S-614G) of the COVID-19 pandemic¹.
40 However, whether the increasing prevalence of the S-614G variant represents a fitness advantage
41 that improves replication and/or transmission in humans or is merely due to founder effects
42 remains elusive. Here, we generated isogenic SARS-CoV-2 variants and demonstrate that the S-
43 614G variant has (i) enhanced binding to human ACE2, (ii) increased replication in primary
44 human bronchial and nasal airway epithelial cultures as well as in a novel human ACE2 knock-in
45 mouse model, and (iii) markedly increased replication and transmissibility in hamster and ferret
46 models of SARS-CoV-2 infection. Collectively, our data show that while the S-614G
47 substitution results in subtle increases in binding and replication *in vitro*, it provides a real
48 competitive advantage *in vivo*, particularly during the transmission bottle neck, providing an
49 explanation for the global predominance of S-614G variant among the SARS-CoV-2 viruses
50 currently circulating.

51 Main Text

52 In late 2019, severe acute respiratory syndrome coronavirus 2 (SARS-CoV-2) emerged in
53 Wuhan, Hubei province, China^{2,3} and rapidly developed into the COVID-19 pandemic. By the
54 end of September 2020, the worldwide death toll had passed one million people with more than
55 37 million infections⁴. Symptoms are usually mild; however in more vulnerable groups, such as
56 aged individuals or people with comorbidities, SARS-CoV-2 can cause life-threatening
57 pneumonia⁵. Cell entry of SARS-CoV-2 is dependent on the interaction of the spike glycoprotein
58 (S) and the host cell surface receptor angiotensin-converting enzyme 2 (ACE2)^{3,6}. S is a
59 homotrimeric class I fusion protein consisting of two subunits S1 and S2, which are separated by
60 a protease cleavage site. The S1 forms a globular head and is essential for receptor binding,
61 while S2 is responsible for fusion of the viral envelope with host cell membranes. During the
62 entry process, the receptor-binding domain (RBD) within the S1 subunit binds ACE2, generating
63 conformational changes in the S2 subunit, which facilitates virus internalization^{7,8}. S-D614G is a
64 protein variant containing a substitution in the S protein outside of the RBD and is thought to
65 cause a conformational change. It is believed to weaken the interprotomer latch in the S protein
66 trimer between the S1 and S2 domains and causes a more “open” conformation that improves
67 ACE2 binding and increases the probability of infection^{1,9}. Over the course of the pandemic, the
68 SARS-CoV-2 S-614G variant rapidly superseded the parental S-614D variant in frequency to
69 become globally dominant. Such a shift in genotype frequency might be caused by a founder
70 effect following introduction into a highly interconnected population. However, there are
71 multiple lines of evidence suggesting that the S-614G variant may confer a fitness advantage
72 compared to S-614D: increased frequency of S-614G in distinct geographical regions, initial
73 experimental evidence with pseudotyped lentiviruses⁹ or vesicular stomatitis viruses⁸, and

74 reports of the S-614G variant being associated with higher viral loads¹. To better address the
75 role that the S-D614G substitution has played in the dissemination and predominance of this
76 SARS-CoV-2 variant during the COVID-19 pandemic, we characterized S protein binding to
77 human ACE2 (hACE2) and replication kinetics *in vitro*, and evaluated infection and transmission
78 dynamics *in vivo* using three different animal models. The data show that the S-D614G
79 substitution confers increased binding to the hACE2 receptor and increased replication in
80 primary human airway epithelial cultures. Moreover, comparison of recombinant isogenic
81 SARS-CoV-2 variants demonstrates that S-614G substitution provides competitive advantage in
82 a hACE2 knock-in mouse model, and markedly increases replication and transmission in Syrian
83 hamster and ferret models.

84

85 **Results**

86 **SARS-CoV-2 S-614G binds to hACE2 more efficiently**

87 To determine whether the S-D614G substitution directly affects the binding between the S and
88 hACE2, we first used the biolayer interferometry (BLI) technology to quantify their biding
89 affinity. Because the S1 component of the S is the domain that interacts with receptor, a
90 reductionist approach was used to determine if the D614G played a role in hACE2 binding by
91 monomeric S1 proteins. Pre-biotinylated polyhistidine-tagged S1 proteins with 614D or 614G
92 (S1-614D and S1-614G, respectively) both bind efficiently to hACE2; however, S1-614G (KD =
93 1.65 nM) showed about 2-fold higher affinity than S1-614D (KD = 3.74 nM) (Figure 1A). When
94 the full-length monomeric spike ectodomain was used in the assay, the S-614G protein also
95 showed higher affinity to hACE2 than S-614D (Extended Data Figure 1A). The enhanced

96 binding to hACE2 protein rendered by the S-D614G substitution also resulted in enhanced S1
97 binding to Baby Hamster Kidney (BHK) cells expressing exogenous hACE2 (BHK-hACE2) in a
98 different binding assay (Figure 1B, Extended Data Figure 1B). We incubated polyhistidine-
99 tagged S1-614D or S1-614G proteins with BHK-hACE2 and analyzed the binding efficiency of
100 S1 to the cells using flow cytometry. At the same S1 concentration, more S1-614G bound to the
101 BHK-hACE2 cells than S1-614D (Figure 1B, Extended Data Figure 1B). Recombinant S1
102 constructs that express two S1 molecules attached to an IgG carboxyl-terminus were generated to
103 further evaluate the impact the S-D614G substitution. An even more striking difference was
104 observed with the pair of Fc(IgG)-tagged S1-614D or S1-614G proteins used for binding studies
105 instead of polyhistidine-tagged S1 constructs (Figure 1B, Extended Data Figure 1B).

106

107 **Increased replication of SARS-CoV-2^{S-614G} virus in primary human epithelial cells**

108 To assess the impact of S-614G in the context of virus infection we generated an isogenic
109 D614G virus pair based on our reverse genetics system for SARS-CoV-2¹⁰. The molecular clone
110 is based on the Wuhan-Hu-1 isolate possessing the S-614D variant (SARS-CoV-2^{S-614D})^{10,11}.
111 The sequence of the isogenic S-614G variant was engineered to have an A to G nucleotide
112 change at position 23,403 to encode a glycine at the S protein position 614. The identity of the
113 resulting recombinant SARS-CoV-2^{S-614G} variant was confirmed by full-length sequencing from
114 the passage 1 virus stock that was used for subsequent experiments. Replication kinetics of
115 SARS-CoV-2^{S-614D} and SARS-CoV-2^{S-614G} in Vero E6 cells marginally differed (Figure 1C). We
116 assessed replication kinetics in primary human nasal epithelial (hNE) and primary normal human
117 bronchial epithelial (NhBE) cultures that were grown under air-liquid interface conditions and
118 resemble the pseudostratified epithelial lining of the human respiratory epithelium. No

119 significant difference in the primary hNE cells following infection of SARS-CoV-2^{S-614D} or
120 SARS-CoV-2^{S-614G} at 33°C, the temperature of the nasal epithelium was observed (Figure 1C). In
121 contrast, SARS-CoV-2^{S-614G} displayed elevated titers in primary NhBE cells at temperatures of
122 33°C, 37°C and 39°C, that resemble temperatures of the upper and lower respiratory tract, or
123 fever, respectively (Figure 1D). Similarly, infection kinetics of NhBE cells with natural isolates
124 SARS-CoV-2/USA-WA1/2020 (USA-WA1, S-614D) or SARS-CoV-
125 2/Massachusetts/VPT1/2020 (MA/VPT1, S-614G) revealed increased titers for the S-614G
126 variant (Extended Data Figure 1C). To refine this analysis, we performed competition
127 experiments by infecting hNE and NhBE cultures with a mixture of both viruses, SARS-CoV-2<sup>S-
128 614D</sup> and SARS-CoV-2^{S-614G}, at defined ratios. In both primary human respiratory culture
129 systems, the ratio of 614G:614D shifted in favor of SARS-CoV-2^{S-614G} during five or eight days
130 of infection (Figure 1E, 1F, Extended Data Figure 1D). Collectively, these results show that the
131 D614G change in the S protein is associated with enhanced hACE2 binding and increased
132 replication in primary human airway epithelial models of SARS-CoV-2 infection.

133

134 **Increased replication of SARS-CoV-2^{S-614G} in hACE2 knock-in mice**

135 Mice do not support efficient replication of SARS-CoV-2 unless they are genetically engineered
136 to express hACE2^{12,13}. To evaluate the relative fitness of the SARS-CoV-2^{S-614G} variant *in vivo*,
137 we generated knock-in mice expressing the authentic SARS-CoV-2 human receptor *hACE2*
138 under the endogenous regulatory elements of the mouse *Ace2* gene (hACE2-KI, Extended Data
139 Figure 2A). Eight heterozygous female mice were inoculated intranasally (i.n.) in a competition
140 experiment with a mixture of both viruses, SARS-CoV-2^{S-614D} and SARS-CoV-2^{S-614G}, using
141 1x10⁵ plaque forming unit (PFU) of each variant (Figure 2A). Viral RNA loads were monitored

142 daily in oropharyngeal swabs and in various organs and tissues by real-time PCR at days 2 and 4
143 post infection (p.i.). No significant body weight loss in hACE2-KI mice up to day 4 p.i. were
144 observed (Extended Data Figure 2B). Longitudinal analysis of daily oropharyngeal swabs
145 revealed efficient virus replication in the upper respiratory tract of hACE2-KI mice (Figure 2B).
146 Accordingly, tissue samples collected at day 2 and 4 p.i. revealed high viral RNA loads in the
147 nasal conchae, lungs and olfactory bulbs and at lower levels in the brain (Extended Data Figure
148 2C). Low to undetectable levels of virus were observed in spleen, small intestine, kidneys and
149 feces (data not shown). No overt pathological lesions were found in the lungs of hACE2-KI
150 compared to wild-type mice at day 2 and 4 p.i. (Extended Data Table 1, 2). Sequencing analysis
151 of the oropharyngeal swabs revealed a net advantage for the SARS-CoV-2^{S-614G} variant over
152 SARS-CoV-2^{S-614D} variant in most animals and time points (Figure 2C). In the organs, a similar
153 replication advantage was found for the SARS-CoV-2^{S-614G} variant (Figure 2D). Collectively,
154 these results demonstrate increased replication of SARS-CoV-2^{S-614G} in a mouse model of SARS-
155 CoV-2 infection in the context of the expression of the authentic human receptor *hACE2*.

156

157 **SARS-CoV-2^{S-614G} displays increased replication and transmissibility in hamsters and
158 ferrets**

159 Hamsters are highly susceptible to SARS-CoV-2 infection and develop disease that closely
160 resembles pan-respiratory, fulminant COVID-19 disease in humans^{14,15}. In contrast, in ferrets
161 SARS-CoV-2 primarily replicates within the upper respiratory tract, resembling mild human
162 infections. However, both animal models efficiently reflect transmission events by direct contact.
163 By using a competition experimental approach *in vivo*, as shown for the hACE2-KI mice,
164 numerical dominance of one recombinant variant should be the result of relevant advantages.

165 Therefore, direct “one-to-one” transmission experiments were conducted. Six donor Syrian
166 hamsters were inoculated i.n. at equal ratios with SARS-CoV-2^{S-614D} and SARS-CoV-2^{S-614G}
167 using $1 \times 10^{4.77}$ TCID₅₀/animal (calculated from back titration of the original material). Analysis
168 of the mixed inoculum by amplicon sequencing and absolute quantification using allele specific
169 locked nucleic acid (LNA) probes confirmed similar viral RNA ratios of both variants (Figure 3).
170 At 24 hours after inoculation, each donor was cohoused with one naive hamster. Weight
171 changes, as well as clinical signs were monitored and nasal washes were collected daily. Viral
172 RNA load in nasal washings, and changes in body weight, were congruent to previously
173 published data^{14,15} (Extended Data Figure 3A, B). Analysis of the viral RNA sequence
174 composition of nasal washings revealed a prominent shift towards SARS-CoV-2S-614G within
175 48 hours post inoculation (Figure 3). Transmission efficiency was one hundred percent, and
176 analysis of the RNA sequence composition showed that the SARS-CoV-2^{S-614G} variant
177 represented >90% of the viral RNA in the contact animals (Figure 3). In summary, hamsters
178 inoculated with both variants, SARS-CoV-2^{S-614D} and SARS-CoV-2^{S-614G}, in an equal ratio,
179 transmit primarily SARS-CoV-2^{S-614G}.

180 To exclude possible differences in hamster's affinity to one variant or divergence of kinetics of
181 the replication cycle six hamsters were inoculated i.n. with either SARS-CoV-2^{S-614D} ($1 \times 10^{5.1}$
182 TCID₅₀/animal, calculated from back titration of the original material), or SARS-CoV-2^{S-614G}
183 ($10^{4.5}$ TCID₅₀/animal, calculated from back titration of the original material) and were monitored
184 for four consecutive days. No marked differences in body weights, titers of shed virus, or viral
185 loads in respiratory tract tissue were observed between the two groups in the acute phase
186 (Extended Data Figure 3C-E). For both variants, highest genome loads were found in the nasal
187 conchae, followed by pulmonary tissue (Extended Data Figure 3E). These observations confirm

188 that in the case of SARS-CoV-2^{S-614D} or SARS-CoV-2^{S-614G} infections, the S-D614G substitution
189 does not seem crucial for clinical outcomes, which again underscores the hamster as a highly
190 sensitive disease model. Rather, the advantage of the SARS-CoV-2^{S-614G} variant over the SARS-
191 CoV-2^{S-614D} has to be adequately large to fully suppress the latter variant within a single *in vivo*
192 replication cycle, which accurately reflects the evolution of SARS-CoV-2^{S-614G} in humans during
193 the COVID-19 pandemic.

194 Since ferrets are a good transmission model¹⁸, we performed a direct “one-to-one” transmission
195 experiment using an equal mixture of the isogenic SARS-CoV-2 variants. Six animals were
196 intranasally inoculated with the mix of SARS-CoV-2^{S-614D} and SARS-CoV-2^{S-614G} ($10^{5.4}$
197 TCID₅₀/animal calculated from back titration of the original material). For all six inoculated
198 ferrets SARS-CoV-2-infection could be confirmed, and both body weight changes and viral
199 RNA loads in nasal washings (Figure 4, Extended Data Figure 4A, B) reflected published
200 data^{16,17}. In five of the six inoculated ferrets, SARS-CoV-2^{S-614G} became the dominant variant
201 (Figure 4). In addition, SARS-CoV-2 transmission occurred in four of the six ferret pairs, and in
202 each pair with successful transmission the S-614G variant prevailed over S-614D (Figure 4). All
203 amplicon sequencing data of the ferret samples were also retested by absolute quantification
204 using allele specific locked nucleic acid (LNA) probes and digital PCR analysis.

205 Notably, the donor of pair one with the dominance of SARS-CoV-2^{S-614D} did not transmit despite
206 a high viral genome peak load of more than 10 million copies per ml. In contrast, the lack of
207 transmission in pair 4 where SARS-CoV-2^{S-614G} became the dominant variant is connected to
208 peak viral loads of below 500,000 genome copies per ml (Figure 4). In summary, the competition
209 experiment in ferrets revealed that the SARS-CoV-2^{S-614G} variant preferentially infected and

210 replicated in five out of six inoculated animals, and transmission events succeeded exclusively
211 with the SARS-CoV-2^{S-614G} variant.

212 **Discussion**

213 SARS-CoV-2 evolution in humans has been proposed to be a non-deterministic process and
214 virus diversification results mainly from random genetic drift, suggesting that there is no strong
215 selective pressure on SARS-CoV-2 in its adaptation to humans²⁰. However, since the
216 introduction of the S-D614G change in early 2020, the SARS-CoV-2 S-614G variant has become
217 globally prevalent¹. A founder effect and a structural change of the SARS-CoV-2 spike protein
218 have been proposed as driving forces establishing the S-614G prevalence. Previous structural
219 studies and the use of pseudotyped viruses have put forward the idea that the S-614G variant
220 may confer increased infectivity, which could be a result of increased “open” RBD conformation
221 for receptor binding as suggested by one study or increased S stability as suggested by another
222 study^{1,9}. In contrast to those studies that used recombinant trimeric S, we used a reductionist
223 approach to eliminate the complications due to the “open” or “closed” RBD conformations in
224 trimeric S. We found the S1 or the monomeric S ectodomain with D614G substitution had
225 increased affinity to hACE2, which may be another mechanism underlying the increased
226 replication and transmission of the SARS-CoV-2 D614G variant.

227 Studies that employed isogenic SARS-CoV-2 D614G variants to assess the phenotype in the
228 context of a SARS-CoV-2 infection were only very recently reported in preprints^{19,20}. Both
229 studies conclude that the SARS-CoV-2 S-614G variant shows increased replication *in vitro* and
230 one study observed earlier transmission in a hamster model. We extended these studies by
231 exploiting various *in vitro* and *in vivo* infection models of SARS-CoV-2, including primary
232 NhBE and hNE cultures, a novel hACE2 knock-in mouse model, a hamster model, and a ferret

233 model. Importantly, throughout these experimental systems we consistently observed an
234 increased fitness of SARS-CoV-2^{S-614G} over SARS-CoV-2^{S-614D} by applying amplicon
235 sequencing techniques as well as allele specific absolute quantification for confirmation. The
236 advantage provided by the D614G change becomes most prominent in competition and
237 transmission experiments in hamsters and ferrets and must therefore be considered as a driving
238 force leading to the global dominance of the SARS-CoV-2 614G variant.

239 Our data are also in agreement with reported functional changes conferred by the D614G
240 substitution in the S protein¹ and infections studies using pseudotyped viruses demonstrating
241 increased infection^{9,21}. Although our studies establish a phenotype of increased replication and
242 transmission of the SARS-CoV-2 S-614G variant, there is no evidence for a phenotypic change
243 in pathogenicity in an animal model. This is important to state, because infection with the SARS-
244 CoV-2 S-614G variant is not associated with the development of severe COVID-19 in humans¹.

245 The ongoing pandemic will likely give rise to additional SARS-CoV-2 variants that may display
246 phenotypic changes and further adaptations to humans. The ability to rapidly trace the genetic
247 variability of emerging variants using whole-genome sequencing, reconstructing emerging virus
248 variants, and assessing their phenotypes will allow rapid response to their emergence with
249 appropriate countermeasures. The development, improvement and characterization of suitable
250 animal models that recapitulate SARS-CoV-2 replication, transmission and pathogenicity in
251 humans will provide a platform to assess the potential implications of these emerging variants.
252 The novel mouse model based on hACE2 expression under the endogenous regulatory elements
253 of the mouse *Ace2* gene will be a valuable tool and will complement existing animal models of
254 SARS-CoV-2 infection. Similarly, as we have shown here, to demonstrate increased replication
255 and transmissibility of SARS-CoV-2^{S-614G}, the phenotypic assessment of future pandemic

256 variants will likely require several complementing animal models that together reflect aspects of
257 SARS-CoV-2 replication, transmission and pathogenicity in humans.

258

259 **Acknowledgements**

260 This work was supported by the Swiss National Science Foundation (SNF; grants
261 31CA30_196644, 31CA30_196062, and 310030_173085), the European Commission (Marie
262 Skłodowska-Curie Innovative Training Network “HONOURS”; grant agreement No. 721367,
263 and the Horizon 2020 project “VEO” grant agreement No. 874735), the Federal Ministry of
264 Education and Research (BMBF; grant RAPID, #01KI1723A) and by core funds of the
265 University of Bern and the German Federal Ministry of Food and Agriculture. The hACE2-
266 KI(B6) KI mice were generated with support from NIH/NIAID P01AI059576 (subproject 5) and
267 partial support from NIH/NIAID U54-AI-057158. Partial support was from the US Centers for
268 Disease Control and Prevention COVID-19 Task Force. We thank the next generation
269 sequencing platform (NGS) of the University of Bern. We also acknowledge Mareen Lange,
270 Christian Korthase, Michael Currier and Gloria Larson and Sandra Renzullo for their excellent
271 technical assistance and Frank Klipp, Doreen Fiedler, Harald Manthei, Christian Lipinski,
272 Jianzhong Tang, and Aurélie Godel for their invaluable support in the animal experiments.

273 This activity was reviewed by CDC and was conducted consistent with applicable federal law
274 and CDC policy: 45 C.F.R. part 46, 21 C.F.R. part 56; 42 U.S.C. Sect. 241(d); 5 U.S.C. Sect.
275 552a; 44 U.S.C. Sect. 3501 et seq. The findings and conclusions in this manuscript are those of
276 the authors and do not necessarily represent the official position of the US Centers for Disease
277 Control and Prevention.

278

279 **Author contributions**

280 VT, DW, MB, and CB conceived the study. TT, BZ, DH, AT performed most of the
281 experiments. NE, SS, FL, JKe, HS, JP, HS, BT, JJ, RD, DH, NJH, LU, JK, AP, BH, XF, XL,
282 LW, NJ, DC, JH, MW, MK, TS, JR, SdB, CB conducted experimental work and/or provided
283 essential experimental systems, data analysis, and reagents. VT, DW, MB, CB, TT, BZ, NE, SS,
284 LT, DH, NJH, LU wrote the manuscript and made the figures. All authors read and approved the
285 final manuscript.

286

287 **Data availability**

288 Sequencing data from passage 1 virus stocks for recombinant SARS-CoV-2^{S-614D} and SARS-
289 CoV-2^{S-614G}, as well as data from all *in vitro* and *in vivo* competition experiments, will be made
290 available on the NCBI Sequence Read Archive (SRA).

291

292 **Competing interests**

293 The authors declare no competing interests.

294

295 **Figure legends**

296 **Figure 1. In vitro characterization of S1 proteins and recombinant SARS-CoV-2^{S-614D} and SARS-**
297 **CoV-2^{S-614G} viruses. (a)** Affinity between S1 and hACE2 determined by Bio-layer interferometry.

298 Biotinylated S1 protein (S1-614D or S1-614G) was loaded onto surface of streptavidin biosensors.
299 Association was conducted using hACE2 protein followed by dissociation. **(b)** Binding of Fc-tagged or
300 polyhistidine-tagged S1 to BHK-hACE2 cells is shown as peaks of fluorescence detected by flow
301 cytometry. **(c)** Replication kinetics of recombinant viruses in (left) Vero E6 at 37°C and (right) hNE at
302 33°C. Supernatant was collected at indicated time points and titrated by plaque assay. Data represent the
303 mean \pm s.d. of three replicates (Vero E6) and four replicates (hNE). **(d)** Replication kinetics of
304 recombinant viruses in NhBE at 33°C (left), 37°C (middle) and 39°C (right). NhBE were infected with
305 100,000 PFU of each virus. Supernatants were collected daily and titrated by TCID50 assay. Data
306 represent the mean \pm s.d. of four replicates. **(c-d)** Statistical significance was determined by two-sided
307 unpaired Student's *t*-test without adjustments for multiple comparisons. **(c)** *P* values (left to right): left,
308 NS, *P*=0.9132; NS *P*=0.0604; NS *P*=0.2394; NS *P*=0.2389; NS *P*=0.2778; NS *P*=0.2781; right, NS
309 *P*=0.1520; NS *P*=0.3891; NS *P*=0.9110; NS *P*=0.8985; NS *P*=0.1464. **(d)** *P* values (left to right): left, NS
310 *P*=0.7943; NS *P*=0.5025; NS *P*=0.6683; NS *P*=0.8985; **P*=0.0220; middle, ***P*=0.0065; NS *P*=0.4660;
311 NS *P*=0.3134; **P*=0.0159; right, ***P*=0.0094; ****P*<10⁻⁴; ***P*=0.0028; ****P*=0.0009. **(e-f)** Competition
312 assay of recombinant viruses in hNE at 33°C and NhBE at 33°C, 37°C and 39°C. The inoculum was
313 prepared by mixing two viruses at 1:1 ratio based on PFU ml⁻¹ and used for infection of hNE and NhBE.
314 Apical wash and supernatant were collected daily, and extracted RNA was used for sequencing. **(e-f)** Bar
315 graph shows proportion of sequencing reads encoding either S-614D or S-614G, and square dots
316 represent individual data points.

317

318 **Figure 2. Replication of SARS-CoV-2^{S-614D} and SARS-CoV-2^{S-614G} viruses in hACE2 knock-in mice.**
319 **(a)** Experimental scheme for infection of hACE2-KI mice intranasally infected recombinant SARS-
320 CoV-2^{S-614D} and SARS-CoV-2^{S-614G} viruses. Oropharyngeal swabs were sampled daily and tissue
321 samples were analyzed in sub-groups of 4 mice at 2 and 4 days post infection (dpi) in two

322 independent experiments. **(b)** Quantitative RT-PCR analysis of oropharyngeal swabs of
323 inoculated hACE2-KI and wild-type mice. **(c,d)** Pie chart representation of mean frequencies of
324 A or G nucleotide at position 23,403 corresponding to SARS-CoV-2^{S-614D} and SARS-CoV-2^{S-}
325^{614G}, respectively. Each pie chart illustrates the ratio of A/G detected from individual
326 oropharyngeal swab samples (c) and tissues (d) at indicated time post infection. OB, olfactory
327 bulb; ND, not detected.

328

329 **Figure 3. Replication and transmission of SARS-CoV-2^{S-614D} and SARS-CoV-2^{S-614G} viruses in**
330 **Syrian hamsters.** Transmission of SARS-CoV-2^{S-614D} and ^{S-614G} variant by hamsters in a pairwise
331 one-by-one setup with direct contact of donor and cohoused contact hamsters is illustrated.
332 Samples of nasal washings were taken daily between days 2 to 8 post infection (dpi) and finally
333 at 12 dpi and were analyzed. Pie chart representation of fraction of A or G nucleotide at position
334 23,403 corresponding to SARS-CoV-2^{S-614D} and SARS-CoV-2^{S-614G}, respectively, measured by
335 amplicon sequencing. Genome copies were calculated from RT-qPCR using a standard RNA.
336 Orange coloring of the hamster silhouette refer to detection of G (SARS-CoV-2^{S-614G}), while
337 blue coloring indicates detection of A (SARS-CoV-2^{S-614D}) on most time points. Grey coloring
338 signals no infection detected

339

340 **Figure 4. Replication and transmission of SARS-CoV-2^{S-614D} and SARS-CoV-2^{S-614G} viruses in**
341 **ferrets.** Schematic illustration of the experimental setup with six pairs of donor ferrets cohoused
342 with naïve contact ferrets. Samples of nasal washings were taken daily between days 2 to 8 post
343 infection (dpi) and finally at 12 dpi and were analyzed. Pie chart representation of fraction of A

344 or G nucleotide at position 23,403 corresponding to SARS-CoV-2^{S-614D} and SARS-CoV-2^{S-614G},
345 respectively. Each pie chart illustrates the ratio of A/G detected from individual nasal washing
346 samples over time. Orange coloring of the ferret silhouette refer to detection of G (SARS-CoV-
347 2^{S-614G}) on most time points, while blue coloring indicates detection of A (SARS-CoV-2^{S-614D}).
348 Numbers represent total genome copies ml⁻¹ and grey coloring signals no infection or viral
349 genome number too low for A/G ratio determination in sequencing. ND, not detected.

350

351 **References**

352 1 Korber, B. *et al.* Tracking Changes in SARS-CoV-2 Spike: Evidence that D614G
353 Increases Infectivity of the COVID-19 Virus. *Cell* **182**, 812-827.e819,
354 doi:10.1016/j.cell.2020.06.043 (2020).

355 2 Zhu, N. *et al.* A Novel Coronavirus from Patients with Pneumonia in China, 2019. *N
356 Engl J Med* **382**, 727-733, doi:10.1056/NEJMoa2001017 (2020).

357 3 Zhou, P. *et al.* A pneumonia outbreak associated with a new coronavirus of probable bat
358 origin. *Nature* **579**, 270-273, doi:10.1038/s41586-020-2012-7 (2020).

359 4 ECDC. *COVID-19 pandemic*, <<https://www.ecdc.europa.eu/en/covid-19-pandemic>>
360 (2020).

361 5 Huang, C. *et al.* Clinical features of patients infected with 2019 novel coronavirus in
362 Wuhan, China. *Lancet* **395**, 497-506, doi:10.1016/s0140-6736(20)30183-5 (2020).

363 6 Letko, M., Marzi, A. & Munster, V. Functional assessment of cell entry and receptor
364 usage for SARS-CoV-2 and other lineage B betacoronaviruses. *Nature Microbiology* **5**,
365 562-569, doi:10.1038/s41564-020-0688-y (2020).

366 7 Wrapp, D. *et al.* Cryo-EM structure of the 2019-nCoV spike in the prefusion
367 conformation. *Science* **367**, 1260-1263, doi:10.1126/science.abb2507 (2020).

368 8 Hoffmann, M. *et al.* SARS-CoV-2 Cell Entry Depends on ACE2 and TMPRSS2 and Is
369 Blocked by a Clinically Proven Protease Inhibitor. *Cell* **181**, 271-280.e278,
370 doi:10.1016/j.cell.2020.02.052 (2020).

371 9 Yurkovetskiy, L. *et al.* Structural and Functional Analysis of the D614G SARS-CoV-2
372 Spike Protein Variant. *Cell*, doi:10.1016/j.cell.2020.09.032 (2020).

373 10 Thi Nhu Thao, T. *et al.* Rapid reconstruction of SARS-CoV-2 using a synthetic genomics
374 platform. *Nature* **582**, 561-565, doi:10.1038/s41586-020-2294-9 (2020).

375 11 Wu, F. *et al.* A new coronavirus associated with human respiratory disease in China.
376 *Nature* **579**, 265-269, doi:10.1038/s41586-020-2008-3 (2020).

377 12 Bao, L. *et al.* The pathogenicity of SARS-CoV-2 in hACE2 transgenic mice. *Nature* **583**,
378 830-833, doi:10.1038/s41586-020-2312-y [pii]10.1038/s41586-020-2312-y [doi] (2020).

379 13 Jiang, R. D. *et al.* Pathogenesis of SARS-CoV-2 in Transgenic Mice Expressing Human
380 Angiotensin-Converting Enzyme 2. *Cell* **182**, 50-58 e58, doi:S0092-8674(20)30622-X
381 [pii]10.1016/j.cell.2020.05.027 [doi] (2020).

382 14 Sia, S. F. *et al.* Pathogenesis and transmission of SARS-CoV-2 in golden hamsters.
383 *Nature* **583**, 834-838, doi:10.1038/s41586-020-2342-5 (2020).

384 15 Imai, M. *et al.* Syrian hamsters as a small animal model for SARS-CoV-2 infection and
385 countermeasure development. **117**, 16587-16595, doi:10.1073/pnas.2009799117 %J
386 Proceedings of the National Academy of Sciences (2020).

387 16 Osterrieder, N. *et al.* Age-Dependent Progression of SARS-CoV-2 Infection in Syrian
388 Hamsters. *Viruses* **12**, doi:v12070779 [pii] viruses-12-00779 [pii] 10.3390/v12070779
389 [doi] (2020).

390 17 Imai, M. *et al.* Syrian hamsters as a small animal model for SARS-CoV-2 infection and
391 countermeasure development. *Proc Natl Acad Sci U S A* **117**, 16587-16595,
392 doi:10.1073/pnas.2009799117 (2020).

393 18 Richard, M. *et al.* SARS-CoV-2 is transmitted via contact and via the air between ferrets.
394 *Nat Commun* **11**, 3496, doi:10.1038/s41467-020-17367-2 (2020).

395 19 Kim, Y. I. *et al.* Infection and Rapid Transmission of SARS-CoV-2 in Ferrets. *Cell Host*
396 *Microbe* **27**, 704-709.e702, doi:10.1016/j.chom.2020.03.023 (2020).

397 20 Alouane, T. *et al.* Genomic Diversity and Hotspot Mutations in 30,983 SARS-CoV-2
398 Genomes: Moving Toward a Universal Vaccine for the “Confined Virus”? *Pathogens* **9**
399 (2020).

400 21 Zhang, J. *et al.* Structural impact on SARS-CoV-2 spike protein by D614G substitution.
401 2020.2010.2013.337980, doi:10.1101/2020.10.13.337980 %J bioRxiv (2020).

402 22 Shi, P. Y. *et al.* Spike mutation D614G alters SARS-CoV-2 fitness and neutralization
403 susceptibility. *Res Sq*, doi:rs.3.rs-70482 [pii]10.21203/rs.3.rs-70482/v1 [doi] (2020).

404 23 Zhang, L. *et al.* The D614G mutation in the SARS-CoV-2 spike protein reduces S1
405 shedding and increases infectivity. *bioRxiv*, doi:2020.06.12.148726
406 [pii]10.1101/2020.06.12.148726 [doi] (2020).

407 24 Li, Q. *et al.* The Impact of Mutations in SARS-CoV-2 Spike on Viral Infectivity and
408 Antigenicity. *Cell* **182**, 1284-1294 e1289, doi:S0092-8674(20)30877-1
409 [pii]10.1016/j.cell.2020.07.012 [doi] (2020).

410 25 van den Worm, S. H. *et al.* Reverse genetics of SARS-related coronavirus using vaccinia
411 virus-based recombination. *PLoS One* **7**, e32857, doi:PONE-D-11-21011
412 [pii]10.1371/journal.pone.0032857 [doi] (2012).
413 26 Thiel, V., Herold, J., Schelle, B. & Siddell, S. G. Infectious RNA transcribed in vitro
414 from a cDNA copy of the human coronavirus genome cloned in vaccinia virus. *J Gen*
415 *Virol* **82**, 1273-1281, doi:10.1099/0022-1317-82-6-1273 [doi] (2001).
416 27 Shepard, S. S. *et al.* Viral deep sequencing needs an adaptive approach: IRMA, the
417 iterative refinement meta-assembler. *BMC Genomics* **17**, 708, doi:10.1186/s12864-016-
418 3030-6 (2016).
419 28 Pasteur, I. Protocol: Real-time RT-PCR assays for the detection of SARS-CoV-2. *WHO*
420 *Document (accessed 10/21/2020):* https://www.who.int/docs/default-source/coronavirus/e/real-time-rt-pcr-assays-for-the-detection-of-sars-cov-2-institut-pasteur-paris.pdf?sfvrsn=3662fcb6_2 (2020).
421
422
423

424 **Methods**

425 **Cell and culture conditions**

426 Vero E6 cells (ATCC) were cultured in Dulbecco's modified Eagle's medium (DMEM)
427 supplemented with 10% fetal bovine serum, 1x non-essential amino acids, 100 units ml⁻¹
428 penicillin and 100 µg ml⁻¹ streptomycin. Baby Hamster Kidney cells expressing SARS-CoV N
429 protein (BHK-SARS-N)²² were maintained in minimal essential medium (MEM) supplemented
430 with 5% fetal bovine serum (FBS), 1x non-essential amino acids, 100 units ml⁻¹ penicillin and
431 100 µg ml⁻¹ streptomycin, 500 µg ml⁻¹ G418 and 10 µg ml⁻¹ puromycin. Twenty-four hours

432 before electroporation, BHK-SARS-N cells were treated with 1 μ g ml⁻¹ doxycyclin to express
433 SARS-CoV N protein. All cell lines were maintained at 37°C and in a 5% CO₂ atmosphere.

434

435 **Recombinant proteins**

436 Recombinant hACE2 protein (Cat: RP01266) was purchased from ABclonal. Recombinant
437 SARS-CoV-2 proteins S1-614D and S1-614G with polyhistidine-tag (Cat: 40591-V08H, 40591-
438 V08H3) were purchased from Sino Biological. All proteins were quantitated with Qubit Protein
439 Assay (Thermo Fisher Scientific). SARS-CoV-2 S1-614D and S1-614G tagged with human IgG
440 Fc fragment were constructed by insertion of the S1 region (residues 1-681) to pFUSE-hIgG1-
441 Fc1 vector (InvivoGen, USA) and expressed using the Expi293 Expression system (Thermo
442 Fisher Scientific). Supernatants were collected and quantified by western blotting using anti-
443 human IgG secondary antibody (ThermoFisher A-21091). SARS-CoV-2 S-614D and S-614G
444 proteins containing polyhistidine- and avi-tagged full-length ectodomain (residues 1-1208, furin
445 cleavage site mutated) was also expressed using the Expi293 Expression system. The full-length
446 ectodomain proteins were purified using HisTrap FF column (GE Life Sciences) in elution buffer
447 containing 20 mM sodium phosphate, 0.5 M NaCl, 500 mM imidazole, pH 7.4, followed by
448 desalting using Zeba spin desalting column (Thermo Fisher Scientific), per manufacturers'
449 instructions. The purified proteins were further concentrated on Amicon Ultra Centrifugal Filters
450 (Sigma-Aldrich) and quantified using Qubit protein assay.

451

452 **Bio-Layer interferometry (BLI) assay**

453 Affinity between human ACE2 to SARS-CoV-2 S1-614D, S1-614G, S-614D or S-614G were
454 evaluated using Octet RED96 instrument at 30°C with a shaking speed at 1000 RPM (ForteBio).
455 Streptavidin biosensors (SA) (ForteBio) were used. S1 proteins were pre-biotinylated using EZ-
456 Link NHS-PEG4-Biotin (ThermoFisher Scientific). Following 20 minutes of pre-hydration of
457 SA biosensors and 1 minute of sensor check, 100 nM S1-614D or S1-614G in 10X kinetic buffer
458 (ForteBio) were loaded onto surface of SA biosensors for 5 minutes. After 2 minutes of baseline
459 equilibration, 10 minutes of association was conducted at 2.5 to 75 nM of human ACE2,
460 followed by 20 minutes of dissociation in the same buffer, which was used for baseline
461 equilibration. S proteins with Avi-tag were pre-biotinylated using BirA biotin-protein ligase
462 standard reaction kit (Avidity). 25 nM S-614D or 15 nM S-614G in 10X kinetic buffer
463 (ForteBio) were loaded onto surface of SA biosensors for 5 minutes. After 2 minutes of baseline
464 equilibration, 5 minutes of association was used for 2 to 32 nM hACE2, followed by 10 minutes
465 of dissociation in 10X kinetic buffer. The data were corrected by subtracting reference sample,
466 1:1 binding model with global fit was used for determination of affinity constants.

467

468 **Flow cytometry**

469 A stable clone of BHK cells expressing exogenous hACE2 were pelleted and resuspended in
470 reaction buffer (PBS pH7.4 with 0.02% tween-20 and 4% BSA) at a concentration of 5×10^6
471 cells/ml. 100 μ l/well of the cells were aliquoted into a round-bottom 96-well plate and incubated
472 on ice for at least 5 min. S1 proteins were diluted in reaction buffer on ice. 50 μ l of S1 diluents
473 were added into corresponding wells of cells and incubated on ice for 20 min with shaking. After
474 incubation, cells were washed in 200 μ l PBST washing solution (PBS pH7.4 with 0.02% tween-
475 20) once and then 100 μ l of 1:300 diluted secondary antibody (ThermoFisher Cat # A-21091 for

476 Fc-tag and ThermoFisher Cat # MA1-21315-647 for polyhistidine-tag) was added into each well
477 of cells, mixed, and incubated on ice with shaking for 15 min. After washing twice, cells were
478 resuspended in 200 μ l PBST and analyzed using the BD FACSCanto II Flow Cytometer. Data
479 was processed with Flowjo_v10.6.1.

480

481 **Generation of infectious cDNA clones using TAR cloning and rescue of recombinant**
482 **viruses**

483 To introduce the 614G mutation to the Spike gene, PCR mutagenesis (Supplementary Table 1)
484 was performed on the pUC57 plasmid containing SARS-CoV-2 fragment 10¹⁰ using Q5® Site-
485 Directed Mutagenesis Kit (New England BioLab). Both D614 and G614 infectious cDNA clones
486 were generated using in-yeast TAR cloning method as describe previously¹⁰. *In vitro*
487 transcription was performed for EagI-cleaved YACs and PCR-amplified SARS-CoV-2 N gene
488 using the T7 RiboMAX Large Scale RNA production system (Promega) as described
489 previously²⁶. Transcribed capped mRNA was electroporated into baby hamster kidney (BHK-21)
490 cells expressing SARS-CoV N protein. Electroporated cells were co-cultured with susceptible
491 Vero E6 cells to produce passage 0 (P.0) of the recombinant S-614D and S-614G viruses.
492 Subsequently, progeny viruses were used to infect fresh Vero E6 cells to generate P.1 stocks for
493 downstream experiments.

494

495 **Virus growth kinetics and plaque assay**

496 Characterization of virus growth kinetics in Vero E6 was performed as described previously¹⁰.
497 Twenty-four hours before infection, cells were seeded in a 24-well plate at a density of 2.0 x 10⁵

498 cells per ml. After washing once with PBS, cells were inoculated with viruses at multiplicity of
499 infection (MOI) of 0.01. After 1 h, the inoculum was removed and cells were washed three times
500 with PBS followed by supply with appropriate culture medium.

501 Plaque forming unit (PFU) per ml of recombinant S-614D and S614-G viruses were determined
502 by plaque assay in a 24-well format. One day before infection, Vero E6 cells were seeded at a
503 density of 2.0×10^5 cells per ml. After washing once with PBS, cells were inoculated with
504 viruses serially diluted in cell culture medium at 1:10 dilution. After 1 h of incubation, inoculum
505 was removed, and cells were washed with PBS and subsequently overlaid with 1:1 mix of 2.4%
506 Avicel and 2X DMEM supplemented with 20% fetal bovine serum, 200 units ml⁻¹ penicillin and
507 200 µg ml⁻¹ streptomycin. After 2 days of incubation at 37°C, cells were fixed in 4% (v/v)
508 neutral-buffered formalin before stained with crystal violet.

509 Statistical significance was determined by two-sided unpaired Student's *t*-test without adjustment
510 for multiple comparisons.

511

512 **Infection of human nasal and bronchial epithelial cells**

513 Primary human nasal epithelial cultures (hNE; MucilAir™ EP02, Epithelix Sàrl, Genève,
514 Switzerland) were purchased and handled according to the manufacturer instructions. Normal
515 human bronchial epithelial (NhBE) cells were purchased (Emory University, Atlanta, GA, USA)
516 and cultured according to recommended protocols. The hNE cultures were inoculated with
517 0.5×10^5 PFU per well, or mixtures of 1:1, 10:1 and 1:10 of SARS-CoV-2^{S-614D} and SARS-CoV-
518 2^{S-614G}. NhBE cell cultures were inoculated with 1.0×10^5 PFU per well, or with wild type isolates
519 SARS-CoV-2/USA-WA1/2020 (USA-WA1, S-614D) or SARS-CoV-

520 2/Massachusetts/VPT1/2020 (MA/VPT1, S-614G) at 2×10^5 TCID₅₀/well, For competition
521 experiments, NhBE cells were inoculated with 1:1 or 9:1 mixed SARS-CoV-2^{S-614D} and SARS-
522 CoV-2^{S-614G} at 1×10^5 PFU per well. After incubation at 33°C for one or two hours, for hNE or
523 NhBE cell cultures respectively, inoculum was removed, cells were washed, and subsequently
524 incubated, as indicated, at 33°C, 37°C, or 39°C. To monitor viral replication, apical washes were
525 collected every 24 hours. All titers were determined by standard plaque-assay or TCID₅₀ on Vero
526 E6 cells.

527 For competition experiments, viral RNA was extracted from apical washes using the QIAamp 96
528 Virus QIAcube HT Kit (QIAGEN). The SARS-CoV-2 genome was amplified using a highly
529 multiplexed tiling PCR reaction based on the ARTIC protocol
530 (<https://www.protocols.io/view/ncov-2019-sequencing-protocol-bbmuik6w>) with some
531 modification. Briefly, primers were designed to produce overlapping 1kb amplicons
532 (Supplementary Table 2). Reverse transcriptase was performed as described in the ARTIC
533 protocol. The single cDNA reaction was carried forward by preparing two PCR reactions, one
534 each for the odd and even pools of primers. Two primer pools (odds and evens) were prepared to
535 contain 0.1 μM of each individual primer. Tiling PCR of the resultant cDNA was performed by
536 combining 12.5 μL 2x Q5 polymerase, 5.5 μL water, 2 μL of the primer pool, and 5 μL of cDNA
537 followed by incubating the reaction at 98°C for 30 seconds, 38 cycles of 98°C for 15 seconds
538 and 63°C for 5 minutes, and holding at 4°C. Corresponding odd and even amplicons were
539 normalized and pool for library preparation. Fragmented libraries were prepared using the
540 Nextera XT DNA library preparation kit and sequenced via Illumina MiSeq. Analyses were
541 performed using IRMA²⁷ with a SARS-CoV-2 module.

542

543 **RNA extraction and RT-PCR**

544 Preparation of viral RNA for next-generation sequencing was performed as described
545 previously¹⁰. In brief, Vero E6 cells were infected with P.1 viruses. Extraction of total cellular
546 RNA was done using Nucleospin® RNA Plus kit (Macherey-Nagel) according to the
547 manufacturers' instruction.

548 RNA from hNE apical washes and mouse oropharyngeal swabs were prepared using QIAamp®
549 Viral RNA Mini Kit (QIAGEN) and Nucleospin® RNA kit (Macherey-Nagel) according to the
550 manufacturers' protocol.

551 To determine the ratios of S-614D:S-614G in competition assays in Epithelix and hACE2-KI
552 mice, reverse transcription PCR was performed on extracted RNA using SuperScript™ IV One-
553 step RT-PCR System (Invitrogen). The sequence-specific primers were used to generate an
554 amplicon of 905 bp covering the D614G region: 5'-AATCTATCAGGCCGGTAGCAC-3' and 5'-
555 CAACAGCTATTCCAGTTAAAGCAC-3'. RT-PCR reaction was performed in a 50- μ l reaction
556 using 0.01 pg to 1 μ g total RNA. The cycling parameters were set as follows: 50°C for 10 min,
557 98°C for 2 min; 35 cycles at 98°C for 10 sec, 55°C for 15 sec, and 72°C for 30 sec; and a 5-min
558 incubation at 72°C. DNA concentration was determined using Qubit dsDNA HS (High
559 Sensitivity) Assay (Thermo Fisher), and subsequently diluted to 200 ng in 50 μ l of nuclease-free
560 water for sequencing by Nanopore sequencing MinION.

561 RNA extraction and preparation of RT-PCR reactions were performed in low- and no-copy
562 laboratory environment to avoid contamination.

563

564 **Sequencing and computational analysis**

565 Recombinant SARS-CoV-2^{S-614D} or SARS-CoV-2^{S-614G} RNAs of P.1 stock were sequenced by
566 next-generation sequencing as described previously¹⁰. Briefly, RNA was extracted from Vero E6
567 cells infected with either recombinant SARS-CoV-2^{S-614D} or SARS-CoV-2^{S-614G} using the
568 NucleoSpin RNA Plus kit (Macherey-Nagel) according to the manufacturer's guidelines.
569 Sequencing libraries were subsequently prepared using the Illumina TruSeq Stranded mRNA
570 Library Prep kit (Illumina, 20020595) and pooled cDNA libraries were sequenced across two
571 lanes on a NovaSeq 6000 S1 flow cell (2 x 50bp, 100 cycles) using the Illumina NovaSeq 6000
572 platform (Next Generation Sequencing Platform, University of Bern, Switzerland). For data
573 analysis, TrimGalore v0.6.5 was used to remove low-quality reads and adaptors from the raw
574 sequencing files. The resulting trimmed paired-end reads were then aligned to the SARS-CoV-2
575 genome (GenBank accession MT108784) using Bowtie2 v2.3.5. Finally, a consensus sequence
576 was generated for each virus stock using Samtools v1.10 with the -d option set to 10,000. Data
577 analysis was performed on UBELIX, the HPC cluster at the University of Bern
578 (<http://www.id.unibe.ch/hpc>).

579

580 **Animal studies:**

581 Ethics declarations.

582 The hACE-2 knock-in mice were originally generated at the Wadsworth Center, New York State
583 Department of Health IACUC protocol # 09-405 (Wentworth, PI). Mouse experimentation was
584 conducted in compliance with the Swiss Animal Welfare legislation and animal studies were
585 reviewed and approved by the commission for animal experiments of the canton of Bern,
586 Switzerland under license BE-43/20. All of the ferret and hamster experiments were evaluated by

587 the responsible ethics committee of the State Office of Agriculture, Food Safety, and Fishery in
588 Mecklenburg-Western Pomerania, Germany (LALLF M-V), and gained governmental approval
589 under registration number LVL MV TSD/7221.3-1- 041/20. This project also obtained clearance
590 from the CDC's Animal Care and Use Program Office.

591

592 Human ACE2 knock-in mouse study.

593 Generation of hACE2 knock-in mice. The hACE2-KI(B6) (B6.Cg-*Ace2*^{tm1(ACE2)Dwnt}/J) line was
594 generated by targeted mutagenesis to express human ACE-2 cDNA in place of the mouse *Ace2*
595 gene. Thus, in this new animal model, hACE2 expression is regulated by the endogenous mouse
596 *Ace2* promoter/enhancer elements. The targeting vector (WEN1-HR) had hACE2 cDNA inserted
597 in frame with the endogenous initiation codon of the mouse *Ace2* (Extended Data Figure 2A).
598 The human cDNA was flanked by an FRT-neomycin-FRT-loxP cassette and a distal loxP site.
599 WEN1-HR was used to transfect 129Sv/Pas ES cells and 837 ES cell clones were isolated and
600 screened for homologous recombination by PCR and Southern blot. Eleven properly recombined
601 ES cell clones were identified and some of them were used for blastocyst injection and
602 implantation into female mice to generate 22 male founders with chimerism
603 (129Sv/Pas:C57BL/6) ranging from 50 to 100%. To complete the hACE2 knock-in, we crossed
604 the chimeric males with C57BL/6J Flp-expressing females to excise the FRT flanked neomycin
605 selection cassette and generate the floxed humanised ACE2 allele (Extended Data Figure 2A).
606 These hACE2 knock-in mice were identified by PCR and confirmed by Southern Blot and were
607 backcrossed to C57BL/6J mice for 7 generations (N7) prior to this study. This line has been
608 donated to The Jackson Laboratory for use by the scientific community (Stock 035000).

609 Heterozygous hACE2-KI female mice were obtained from The Jackson Laboratory (USA) and
610 C57BL/6J wild-type (WT) female mice were from Janvier Lab (France). All mice were
611 acclimatized for at least 2 weeks in individually ventilated cages (blue line, Tecniplast), with
612 12/12 light/dark cycle, autoclaved acidified water, autoclaved cages including food, bedding and
613 environmental enrichment at the SPF facility of the Institute of Virology and Immunology,
614 Mittelhäusern, Switzerland. One week before infection, mice were placed in individually HEPA-
615 filtered isolators (IsoCage N, Tecniplast). Mice (10-12-week-old) were anesthetized with
616 isoflurane and infected intranasally with 20 μ l (i.e., 10 μ l per nostril) with a 1:1 ratio of the
617 SARS-CoV-2 variants (WT and hACE2-KI mice) or mock culture medium (WT mice only).
618 After intranasal infection, mice were monitored daily for body weight loss and clinical signs.
619 Throat swabs were collected daily under brief isoflurane anesthesia using ultrafine sterile flock
620 swabs (Hydraflock, Puritan, 25-3318-H). The tips of the swabs were placed in 0.5 mL of RA1
621 lysis buffer (Macherey-Nagel, Ref. 740961) supplemented with 1% β -mercaptoethanol and
622 vortexed. Groups of mice from two independent experiments were euthanized on days 2 and 4
623 p.i. and organs were aseptically dissected avoiding cross-contamination. Systematic tissue
624 sampling was performed: (1) lung right superior lobe, right nasal concha, right olfactory bulb,
625 part of the right brain hemisphere, apical part of the right kidney, parts of the distal small
626 intestine (ileum) were collected for RNA isolation in RA1 lysis buffer; (2) lung middle, inferior
627 and post-caval lobes, left nasal concha, left olfactory bulb, part of the right brain hemisphere,
628 part of the right kidney were collected in MEM; (3) lung left lobe, liver left lobe, left kidney, left
629 brain hemisphere and part of the jejunum and ileum were fixed in buffered formalin. Data were
630 generated from two identically designed independent experiments.

631 Mouse tissue samples collected in RA1 lysis buffer supplemented with 1% β -mercaptoethanol
632 were homogenized using a Bullet Blender Tissue Homogenizer (Next-Advance). Homogenates
633 were centrifuged for 3 min at 18,000 g and stored at -70°C until processing. Total RNA was
634 extracted from homogenates using the NucleoMag VET kit for viral and bacterial RNA/DNA
635 from veterinary samples (Macherey Nagel, Ref: 744200) and the KingFisher Flex automated
636 extraction instrument (ThermoFisher Scientific) following manufacturers' instructions. RNA
637 purity was analyzed with a NanoDrop 2000 (ThermoFisher Scientific). A 25 μ l RT-PCR for the
638 viral E gene was carried out using 5 μ l of extracted RNA template using the AgPath-ID One-
639 Step RT-PCR (Applied Biosystems). Samples were processed in duplicate. Amplification and
640 detection were performed in a Applied Biosystem 7500 Real-Time PCR Systems under the
641 following conditions: an initial reverse transcription at 45 °C for 10 min, followed by PCR
642 activation at 95 °C for 10 min and 45 cycles of amplification (15 seconds at 95 °C, 30 seconds at
643 56 °C and 30 seconds at 72 °C). Relative quantification of virus load in swabs and mouse tissues
644 was based on β 2 microglobulin expression measured by TaqMan qPCR according to the
645 manufacturer's protocol (Assay mM00437762_m; ThermoFisher).

646 Fixed mouse tissue samples were processed, sectioned and stained with hematoxylin and eosin
647 (H&E) at the COMPATH core facility (University of Bern). Histopathological lung slides of
648 hACE2-KI mice and wild-type mice (infected and mock) were examined and scored by a board-
649 certified veterinary pathologist (SdB), who was blinded to the identity of the samples. Scoring
650 criteria are detailed in Extended Data Table 2.

651

652 Hamster study

653 Six Syrian hamsters, *Mesocricetus auratus*, (Janvier Labs, France) were infected intranasally
654 under a short-term inhalation anesthesia with 70 μ l of SARS-CoV-2^{S-614D} and SARS-CoV-2^{S-614G}
655 at equal ratios using $10^{4.77}$ TCID₅₀/animal (calculated from back titration of the original
656 material). After 24 hours of isolated housing in individually ventilated cages (IVCs), six pairs,
657 each with one directly inoculated donor hamster and one sham-inoculated contact hamster were
658 co-housed. The housing of each hamster duo was strictly separated in individual cage systems to
659 prevent spill-over between different pairs. For the following seven days (day 2 until day 8 after
660 infection) and on day 12 after infection, viral shedding was monitored in addition to a daily
661 physical examination and body weighting routine.

662 To evaluate viral shedding, nasal washes were individually collected from each hamster under a
663 short-term isoflurane anesthesia. Starting with the pair's contact hamster, each nostril was rinsed
664 with 100 μ l PBS (1.0x phosphate-buffered saline) and reflux was immediately gathered. A new
665 pipet tip for every nostril and hamster was used to prevent indirect spill-over transmission from
666 one animal to another. Furthermore, in-between the respective pairs, a new anesthesia system
667 was used for each pair of animals. At day 8 post infection, one contact hamster was found dead.
668 Although having lost up to almost 20% of their body weight, every other hamster recovered from
669 disease. Under euthanasia, serum samples were collected from each hamster.

670 For a second experimental setup seven hamsters each were infected via the intranasal route with
671 $10^{5.1}$ TCID₅₀/animal of SARS-CoV-2^{S-614D}, or $10^{4.5}$ TCID₅₀/animal SARS-CoV-2^{S-614G}
672 (calculated from back titration of the original material). From day 1 onwards to day 4 nasal
673 washes were obtained from these hamsters and body weight changes recorded. A tissue panel
674 from respiratory organs, including nasal conchae, tracheal tissue, cranial, medial, and caudal

675 portions of the right lung, and the pulmonary lymph node, were collected after euthanasia from
676 these hamsters.

677

678 Ferret study

679 In accordance with the hamster study, twelve ferrets (*Mustela putorius furo*) from in-house
680 breeding, were divided into six groups of two individuals. Ferret pairs were of equal age between
681 four and 18 months. In total, four ferrets were female (two pairs) and eight ferrets were male or
682 neutered male (four pairs). The housing of each ferret duo was strictly separated in individual
683 cage systems, to prevent spill-over between different pairs. Per separate cage, one individual
684 ferret was inoculated intranasally, by instillation of 125 μ l of the aforementioned inoculum
685 (1x10⁵ TCID₅₀/animal; calculated from back titration of the original material) into each nostril
686 under a short-term isoflurane-based inhalation anesthesia. Time points and sampling technique
687 corresponded to the methods used for the hamsters, albeit ferret nasal washing was performed
688 using two times 700 μ l PBS per animal. The contact-ferret was not inoculated.

689

690 Specimen work-up, viral RNA detection, sequencing and quantification analyses

691 Organ samples were homogenized in a 1 ml mixture of equal volumes composed of Hank's
692 balanced salts minimum essential medium (MEM) and Earle's balanced salts MEM containing 2
693 mM l-glutamine, 850 mg l-1 NaHCO₃, 120 mg l-1 sodium pyruvate and 10% FCS
694 (supplemented with 10% Fetal Calf Serum and 1% penicillin-streptomycin) at 300 Hz for two
695 minutes using the Tissuelyser II (Qiagen, Hilden, Germany) and centrifuged to clarify the
696 supernatant. Nucleic acid was extracted from 100 μ l of the nasal washes after a short

697 centrifugation step or organ sample supernatant using the NucleoMag Vet kit (Macherey Nagel,
698 Düren, Germany). Viral loads in these samples were determined using the nCoV_IP4 RT-PCR²⁸
699 including standard RNAs that were absolute quantified by digital droplet PCR with a sensitivity
700 of 10 copies/reaction. The extracted RNA was afterwards subjected to MinION sequencing and
701 digital droplet PCR. For MinION sequencing, amplicons were produced with primers (WU-21-F:
702 AATCTATCAGGCCGGTAGCAC; WU-86-R: CAACAGCTATTCCAGTTAAAGCAC) using
703 SuperScript IV One-step RT-PCR (Thermo Fisher Scientific; Waltham, MA USA). Amplicons
704 were sequenced on a MinION system using from Oxford Nanopore using Native Barcoding 1-12
705 (EXP-NBD104) and 13-24 (EXP-NBD114), respectively with Ligation Kit SQK-LSK109
706 (Oxford Nanopore; Oxford, UK). Libraries were loaded on R9.4.1 Flow Cells (FLO-MIN106D)
707 on a MinION coupled to a MinIT. Realtime high accuracy basecalling, demultiplexing and
708 barcode and adapter trimming was performed with MinKnow v20.06.17, running Guppy
709 vs4.0.11. Downstream analysis was done in Geneious 2019 vs2.3. Read length filtered
710 eliminated reads < 800 and > 1100 nt and remaining reads were mapped in subsets of 10,000
711 reads to the amplicon reference undergoing two iterations, with custom sensitivity allowing a
712 maximum of 5% gaps and maximum mismatch 30%. Variants were analyzed on specific position
713 with calculating p-values for every variant. Ratio fraction A/G was calculated from numbers of
714 reads as fraction=Areads/(Areads+Greads).

715 For rare mutation and sequence analysis based on digital PCR, the QX200 Droplet Digital PCR
716 System from Bio-Rad (Hercules, CA, USA) was used. For RT-PCR, the One-Step RT-ddPCR
717 Advanced Kit for Probes (Bio-Rad) was applied according to the supplier's instructions. For the
718 amplification of an 86 bp fragment of both variants of the spike protein gene, the forward primer
719 SARS2-S-1804-F (5'-ACA AAT ACT TCT AAC CAG GTT GC-3') and the reverse primer

720 SARS2-S-1889-R (5'-GTA AGT TGA TCT GCA TGA ATA GC-3') were used. For the
721 detection of the D and G variants in one sample, two allele specific locked nucleic acid (LNA)
722 probes were applied: SARS2-S-v1D-1834FAM (5'-FAM-TaT cAG gat GTt AAC-BHQ1-3') and
723 SARS2-S-v3G-1834HEX (5'-HEX-T cAG ggt GTt AAC-BHQ1-3'). The LNA positions are
724 depicted in lower case. The concentration of the primers and probes was 20 μ M and 5 μ M,
725 respectively. For data analysis, the QuantaSoft Analysis Pro software (version 1.0.596) was used.

726

727 **Extended Data Fig. 1. Additional *in vitro* characterization of S proteins and SARS-CoV-2^{S-614D}**
728 **and SARS-CoV-2^{S-614G} isolates.**

729 **(a)** Affinity between S and hACE2 determined by Bio-layer interferometry. Biotinylated spike
730 protein (ectodomain) (S-614D or S-614G) was loaded onto surface of streptavidin biosensors and
731 association was conducted using hACE2 followed by dissociation. Data represent two biological
732 replicates. **(b)** Binding of Fc-tagged or polyhistidine-tagged S1 to BHK-hACE2 cells determined
733 by flow cytometry. Mean Fluorescence intensity is shown for corresponding S1 protein
734 concentration. Data represent the mean \pm s.d. of three biological replicates. **(c)** Replication of
735 wild type SARS-CoV-2/USA-WA1/2020 (S-614D) and SARS-CoV-
736 2/Massachusetts/VPT1/2020 (S-614G) isolates in NhBE cells at 33°C (left), 37°C (middle), and
737 39°C (right). NhBE cells were infected with 200,000 TCID50 of each virus. Supernatants were
738 collected every 24 h and titrated by TCID50 assay. Data represent the mean \pm s.d. of four
739 replicates. Statistical significance was determined by two-sided unpaired Student's *t*-test without
740 adjustments for multiple comparisons. *P* values (from left to right): left, NS *P* = 0.7874; **P* =
741 0.0328; NS *P* = 0.1887; NS *P* = 0.8985; NS *P* = 0.5296; middle, NS *P* = 0.1475; NS *P* = 0.1415;
742 ** *P* = 0.0033; NS *P* = 0.3184; right, NS *P* = 0.6018; NS *P* = 0.3903; NS *P* = 0.0898; **P* =

743 0.0445. **(d)** Competition assay of recombinant SARS-CoV-2^{S-614D} and SARS-CoV-2^{S-614G} in
744 NhBE at 33°C, 37°C and 39°C. The inoculum was prepared by mixing two viruses at 9:1 ratio
745 based on plaque forming unit ml⁻¹. NhBE was infected with 100,000 pfu of the 9:1 virus mix.
746 Viral RNA was extracted from daily supernatant and sequenced by next generation sequencing.
747 Bar graph shows proportion of sequencing reads encoding either S-614D or S-614G, and each
748 square dot represents one individual data point.

749

750 **Extended Data Figure 2. hACE-2 KI mouse generation and infection with SARS-CoV-2^{S-}**
751 **^{614D} and SARS-CoV-2^{S-614G} viruses.** **(a)** Design and generation of humanized ACE2 knock-in
752 mice (hACE2-KI). The hACE2 cDNA was inserted in frame with the endogeneous initiation
753 codon of mouse Ace2 in exon 2, which was deleted. The hACE2 cDNA was flanked 5' with a
754 loxP site (black triangle) and 3' with a FRT-neomycin-FRT-loxP cassette. The targeting
755 construct included a negative selection cassette (PGK-DTA) to improve selection of clones with
756 homologous recombination. Chimeric male mice transmitting the targeted locus were crossed
757 with Flp-deleter female mice to generate the floxed hACE2 knock-in allele. This allele can be
758 used : (1) without further cre-mediated recombination, as shown here, to study humanized ACE2
759 mice (hACE2-KI), where the hACE2 cDNA is expressed in place of mouse Ace2; (2) after
760 crossing with a cre-deleter mouse line to generate constitutive *Ace2* knock-out mice; (3) after
761 crossing with tissue-specific cre line. Ubiquitous and tissue-specific knock-out mice can be
762 crossed with conventional hACE2 transgenic mice to remove the endogenous mouse ACE2,
763 which could confound pathogenesis studies that may occur due to heterodimerization of ACE2.
764 **(b)** Body weight loss at indicated time points after infection of hACE2-KI mice (n=8), wild-type
765 mice infected (n=9) and for mock-infected wild-type sampled identically (n=10). **(c)** Quantitative

766 RT-PCR analysis of tissue homogenates of inoculated hACE2-KI and wild-type mice at
767 indicated time points.

768

769 **Extended Data Figure 3. Virus replication in infected Syrian hamsters.**

770 **(a)** Body weight loss at indicated time points after infection of Syrian hamsters. Donor animals
771 (n=6; black dots) were intranasally inoculated with SARS-CoV-2^{S-614D} / SARS-CoV-2^{S-614G} at
772 equal ratio (1x10^{4.77} TCID₅₀/animal as determined by backtitration of the original inoculum).
773 24h after infection, naïve hamsters (n=6; orange triangles) were housed in direct contact in an
774 “one-to-one” experimental setup. **(b)** Quantitative RT-PCR analysis of individual nasal washing
775 samples obtained from donor hamsters and contact animals, respectively. **(c)** Body weight loss at
776 the indicated time points after infection of the hamsters. Syrian hamsters were inoculated with
777 10^{5.1} TCID₅₀/animal of SARS-CoV-2^{S-614D} (n=7, blue dots), or 10^{4.5} TCID₅₀/animal SARS-CoV-
778 2^{S-614G} (n=7, red triangles) via the intranasal route. Titers were determined by backtitration of the
779 original inoculation material. **(d)** Viral genome copy numbers are shown as determined by RT-
780 qPCR from individual nasal washing samples of the animals inoculated with the single variant
781 virus. **(e)** Quantitative RT-PCR analysis of tissue homogenates of inoculated hamsters of the
782 SARS-CoV-2^{S-614D} group (n=7, blue dots) versus the SARS-CoV-2^{S-614G} group (n=7, red
783 triangles).

784

785 **Extended Data Figure 4. “Twin”-inoculation of donor ferrets with equal ratios of SARS-**
786 **CoV-2^{S-614D} and SARS-CoV-2^{S-614G}.**

787 Donor ferrets (black dot; n=6) were intranasally inoculated with $10^{5.4}$ TCID₅₀/animal as
788 determined by back titration of an inoculum comprising equal ratios of SARS-CoV-2^{S-614D} and
789 SARS-CoV-2^{S-614G}. Twenty four hours post inoculation one contact ferret (orange triangle; n=6)
790 was commingled with one donor ferret, creating six donor – contact ferret pairs. **(a)** Individual
791 body weight of ferrets at the indicated days, relative to the day of inoculation, is plotted. **(b)**
792 Genome copy numbers for inoculated donor and contact ferrets. Individual nasal washing
793 samples of the indicated days were analyzed by RT-qPCR “nCoV_IP4”, and absolute numbers
794 were calculated using a set of standard RNAs. All donor ferrets (black dots) tested vRNA
795 positive, starting already day 2 post inoculation (n=6). 4 out of 6 contact ferrets (orange
796 triangles) tested vRNA positive beginning with day 4 (corresponding with day 3 after contact). 2
797 of the 6 contact ferrets never tested positive for vRNA throughout the study.

798

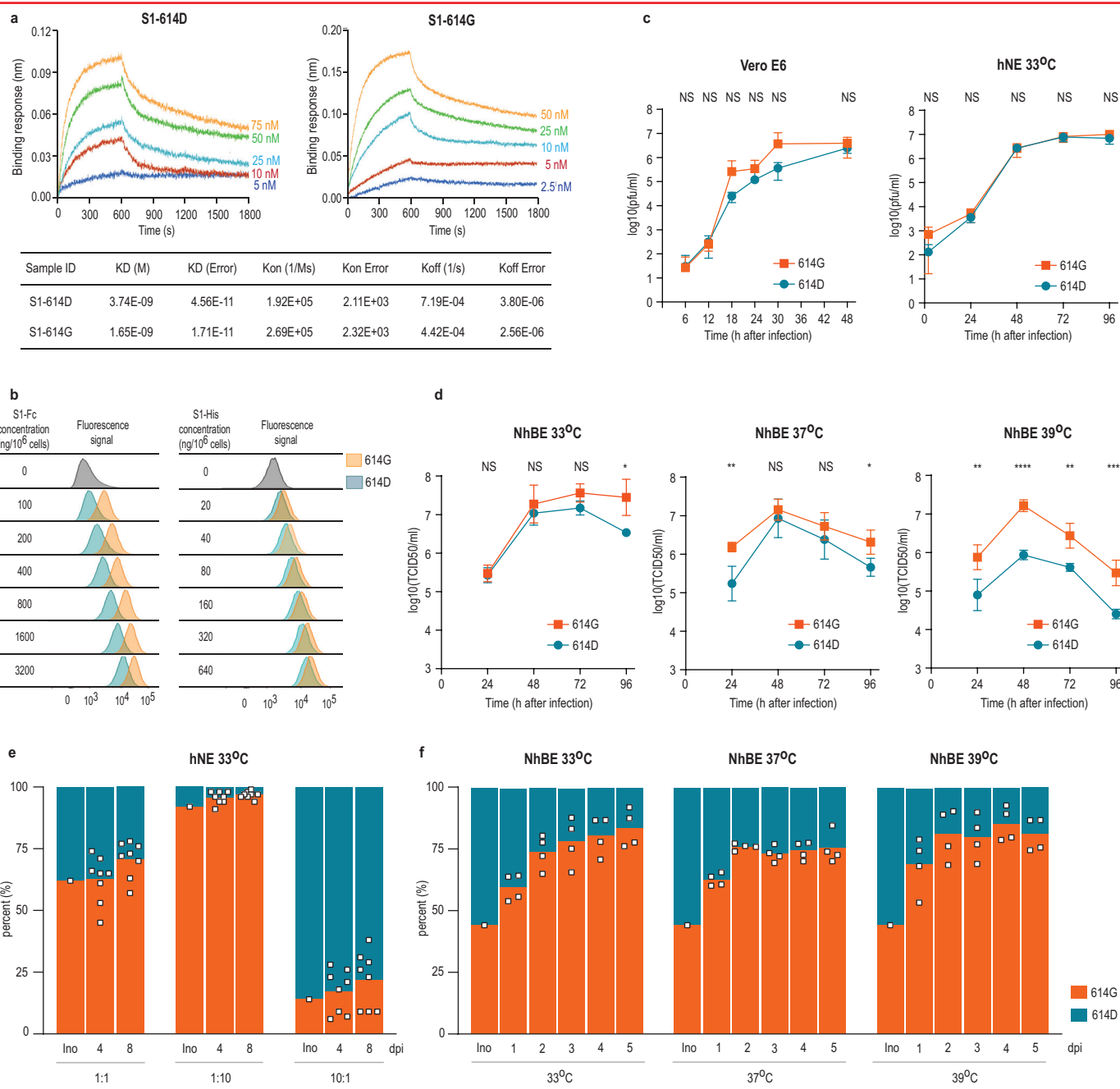
799 **Extended Data Table 1 | Lung histopathological score of mice infected with SARS-CoV-2.**
800 Data is shown for individual hACE2-KI mice (K1-K8) and wild-type inoculated (WT1-WT9)
801 and wild-type mice mock inoculated (M1-M10). Scoring criteria are detailed in Extended Data
802 Table 2. Scoring was performed by a pathologist blinded sample identification.

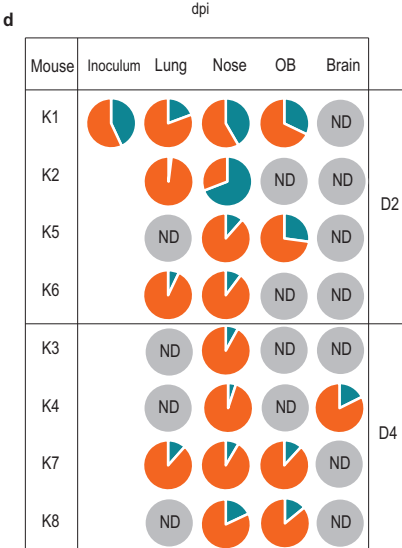
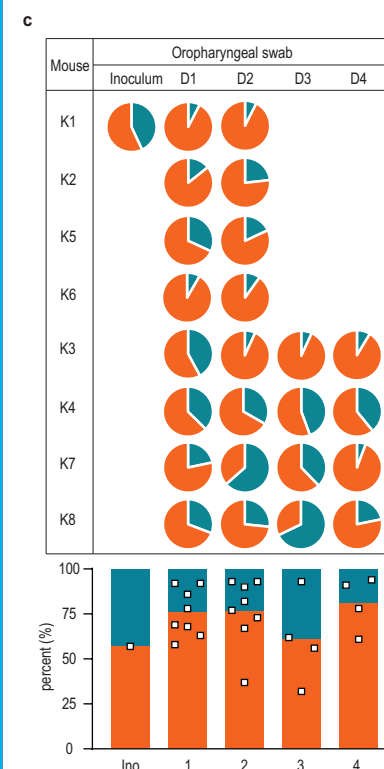
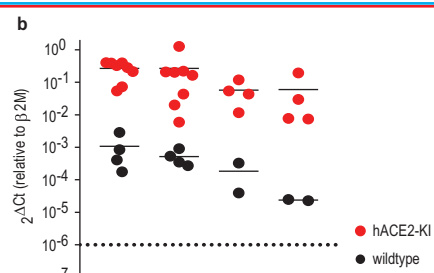
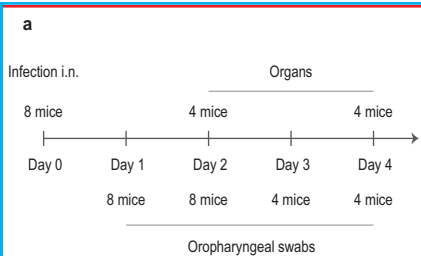
803

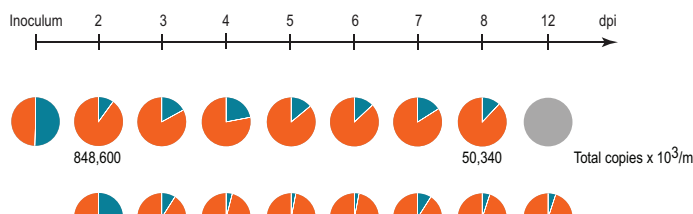
804 **Extended Data Table 2 | Score sheet of lung histopathology.**

805

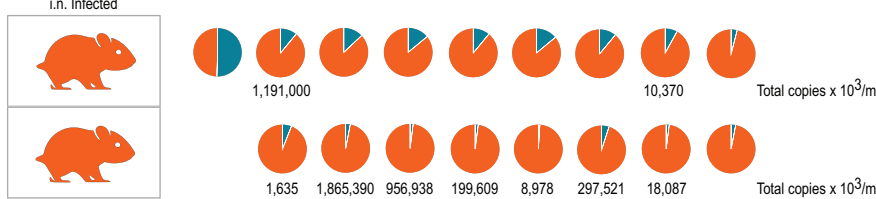
806



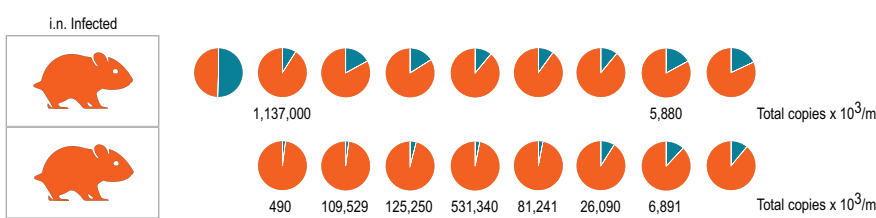




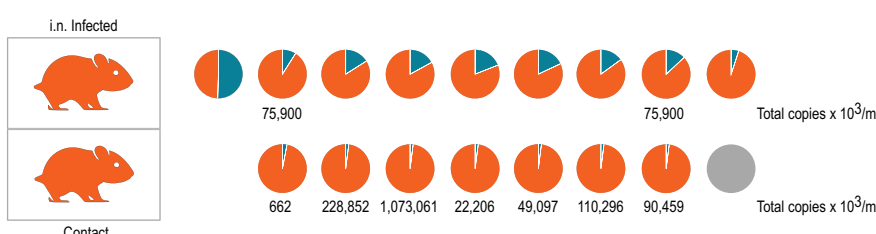
Pair 1



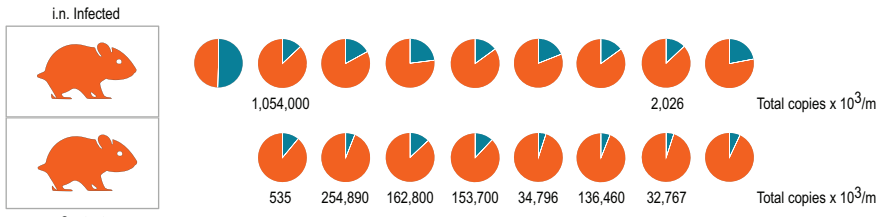
Pair 2



Pair 3



Pair 4



Pair 5



Pair 6



Inoculum 2 3 4 5 6 7 8 12 dpi

